

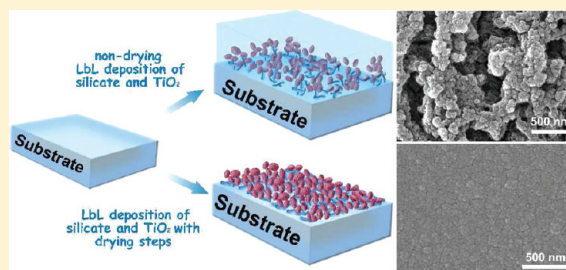
Drying and Nondrying Layer-by-Layer Assembly for the Fabrication of Sodium Silicate/TiO₂ Nanoparticle Composite Films

Lianbin Zhang, He Liu, Engui Zhao, Lingying Qiu, Junqi Sun,* and Jiacong Shen

State Key Laboratory of Supramolecular Structure and Materials, College of Chemistry, Jilin University, Changchun, 130012, P. R. China

Supporting Information

ABSTRACT: Influences of drying and nondrying steps on structures of layer-by-layer (LbL) assembled sodium silicate/TiO₂ nanoparticles films (denoted as silicate/TiO₂ films) have been systematically investigated. The nondrying LbL assembly produces highly porous silicate/TiO₂ films with large thickness. In contrast, the silicate/TiO₂ films fabricated with a drying step after each layer deposition are flat and thin without porous structures. In situ atomic force microscopy (AFM) measurements confirm that the sodium silicate and TiO₂ nanoparticles are deposited in their aggregated forms. A N₂ drying step can disintegrate the aggregated silicate and TiO₂ nanoparticles to produce thin silicate/TiO₂ films with compact structures. Without the drying steps, the aggregated silicate and TiO₂ nanoparticles are well retained, and their LbL assembly produces highly porous silicate/TiO₂ films of large thickness. The highly porous silicate/TiO₂ films are demonstrated to be useful as reusable film adsorbents for dye removal from wastewater because they can adsorb a large amount of cationic organic dyes and decompose them under UV irradiation. The present study is meaningful for exploring drying/nondrying steps for tailoring structure and functions of LbL assembled films.



INTRODUCTION

Interest in the layer-by-layer (LbL) assembly technique, which involves the alternate deposition of species with complementary chemical interactions for the fabrication of composite films,^{1,2} has been continuously growing because LbL assembled films have multiple applications in areas such as nonlinear optics,³ superhydrophobic surfaces,⁴ biosensors,⁵ drug delivery systems,⁶ smart films,⁷ and so forth. The LbL assembly allows a broad range of materials including synthetic polymers, particles,⁸ biomacromolecules,⁹ oligo-charged organic molecules,¹⁰ polymeric complexes,¹¹ and so forth to be alternately assembled on various substrates based on multiple weak interactions. Compared with other film-preparation methods, the LbL assembly is unique in precisely controlling the chemical composition and structure of the films on micro- and nanoscales because all species are deposited in a predesigned LbL fashion.² Meanwhile, the LbL assembly is particularly suitable for film fabrication on nonflat surfaces with large areas.¹² These merits make the LbL assembly promising for large-scale production of functional composite films.^{2–7} In the past two decades, parameters capable of tailoring the structures of the LbL assembled films including temperature,¹³ ionic strength,¹⁴ concentration,¹⁵ and pH¹⁶ of dipping solutions have been systematically studied and employed for the fabrication of various kinds of functional films. Take the LbL assembly of oppositely charged species for instance; the processes for multilayer film fabrication usually involve repeated, sequential immersion of a substrate into aqueous solutions of oppositely charged materials with intermediate

water rinsing and nitrogen drying steps. Although the drying step is usually conducted after each layer deposition, it can be omitted to simplify the LbL assembly processes, especially when robots are used for multilayer film construction.¹⁷ However, compared with parameters mentioned above, the drying/nondrying steps have not been purposely explored to tailor the structure of the LbL assembled films.

Previous studies show that the drying/nondrying steps can produce influences on thickness, roughness, and surface defects of LbL assembled polyelectrolyte multilayer films.^{18,19} However, the structural difference caused by the drying/nondrying steps is generally slight and cannot be effectively employed to tailor film structures and functions.¹⁸ Meanwhile, the mechanism under which the drying/nondrying steps affect the film structure is still full of controversy and needs to be clarified.¹⁸ For instance, the slight structural difference for drying and nondrying LbL assembled polyelectrolyte multilayer films is difficult to detect.¹⁹ By using charged Au nanoparticles as probes, Su and co-workers disclose that intermediate drying with nitrogen flow can reduce surface defects in LbL assembled poly(diallyldimethylammonium chloride) (PDAA)/poly(sodium 4-styrenesulfonate) (PSS) films.¹⁹ However, the difference of surface defects between PDAA/PSS films fabricated with and without drying steps becomes less obvious with more layers deposited. Our recent work shows that the

Received: November 3, 2011

Revised: December 19, 2011

Published: December 21, 2011

drying/nondrying steps can produce a dramatic influence on structure of the LbL assembled polymeric films composed of alternately deposited polymeric complexes.^{11d–f} For example, nondrying LbL assembly of negatively charged polyelectrolyte complexes (PECs) of poly(acrylic acid) (PAA) and diazoresin (DAR) (noted as PAA-DAR) with positively charged PECs of DAR and PSS (noted as DAR-PSS) enables the rapid fabrication of micrometer-thick PAA-DAR/DAR-PSS foam films. A 15-bilayer PAA-DAR/DAR-PSS film has a thickness of $\sim 1.8\ \mu\text{m}$. However, the LbL assembled 15-bilayer PAA-DAR/DAR-PSS film with drying steps after each layer deposition is compact and has a thickness of $\sim 130\ \text{nm}$.^{11d}

In the present study, we prove that building blocks with proper rigidity and dimensions are required to amplify the influence of drying/nondrying steps on structures of LbL assembled films. To do so, sodium silicate and TiO_2 nanoparticles are alternately deposited by the nondrying and drying LbL assembly to prepare sodium silicate/ TiO_2 nanoparticles films (denoted as silicate/ TiO_2 films). In situ atomic force microscopy (AFM) measurements confirm that sodium silicate and TiO_2 nanoparticles are deposited in their aggregated forms. The alternate deposition of the rigid aggregates of silicate and TiO_2 nanoparticles by the nondrying LbL assembly leads to the loose deposition of silicate and TiO_2 nanoparticles and therefore produces highly porous silicate/ TiO_2 films with large thickness. In contrast, the drying LbL assembly produces thin silicate/ TiO_2 films with compact structures because the N_2 drying step can disintegrate the aggregated silicate and TiO_2 nanoparticles. As an example of application, we demonstrate that the porous silicate/ TiO_2 films have a high capability of removing organic dyes from wastewater. The present study is meaningful for understanding the correlation between rigidity and dimension of building blocks and tunability of film structure by drying/nondrying steps and for exploring drying/nondrying steps for tailoring structure and functions of LbL assembled films.

EXPERIMENTAL SECTION

Materials. Poly(diallyldimethylammonium chloride) (PDPA, 20 wt %, M_w ca. 100 000–200 000), titanium(IV) isopropoxide (97%), poly(acrylic acid) (PAA, M_w 1800), and sodium silicate were all purchased from Sigma-Aldrich and used as received. Water purified in a Milli-Q (Milli Pore) system was used during all the experiments.

Synthesis of TiO_2 Nanoparticles. TiO_2 nanoparticles were synthesized by the controlled hydrolysis of titanium isopropoxide according to a literature method.²⁰ Simply, 2.5 mL of titanium isopropoxide dissolved in 50 mL of absolute ethanol was added dropwise under vigorous stirring to 500 mL of distilled water ($4\ ^\circ\text{C}$) adjusted to pH 1.5 with nitric acid. The resulting transparent colloidal suspension (2.0 mg/mL) was stirred overnight. The colloidal suspension was stored at a temperature of ca. $4\ ^\circ\text{C}$.

Fabrication of Silicate/ TiO_2 Composite Films. Quartz slides and silicon wafers were immersed in a slightly boiled piranha solution (3:1 mixture of 98% H_2SO_4 and 30% H_2O_2) for 20 min and rinsed with copious amounts of water and dried with N_2 flow. *Caution: piranha solution reacts violently with organic materials and should be handled carefully.* The freshly cleaned substrates of quartz slides or silicon wafers were first immersed in aqueous PDPA solution (1.0 mg/mL) for 20 min to render the substrate positively charged, followed by rinsing with water and drying with N_2 flow. Then sodium silicate and TiO_2 composite films were deposited on the PDPA-modified substrates. For the nondrying LbL assembled films, the substrate was first immersed in a solution of sodium silicate (0.154 M, pH = 11.4) for 10 min, followed by rinsing in three water baths for 1 min each. Then the substrate was immediately transferred to TiO_2

colloidal suspension (2.0 mg/mL, pH = 2.5) for 10 min, followed by rinsing in three water baths for 1 min each. By repetition of the above deposition process in a cyclic fashion, silicate/ TiO_2 composite films can be prepared. No drying step was used in the deposition procedure unless it was in the last layer. The nondrying LbL assembled silicate/ TiO_2 films with n cycle deposition are denoted as (silicate/ TiO_2)* n_{ND} , where ND next to the number of deposition cycles represents nondrying steps. For the drying LbL assembled films, the same deposition and rinsing procedures were conducted for the layers of silicate and TiO_2 nanoparticles, except a N_2 flow was performed after substrate was rinsed with water. The drying LbL assembled silicate/ TiO_2 films with n cycle deposition are denoted as (silicate/ TiO_2)* n_{D} , with D representing drying steps. If not specifically stated, the silicate/ TiO_2 films are fabricated using aqueous sodium silicate solution of 0.154 M.

Characterization. UV–vis absorbance measurements were conducted using a Shimadzu UV-2550 spectrophotometer. Scanning electron microscopy (SEM) images were obtained on a XL30 ESEM FEG scanning electron microscope. The measurements of film thicknesses were obtained from their cross-sectional SEM images. The mean value of thickness was gathered by averaging at least five individual positions of a sample. The energy-dispersive X-ray spectroscopy (EDX) measurement was conducted on an EDAX Genesis 2000 X-ray microanalysis system attached to an XL30 ESEM FEG scanning electron microscope. Transmission electron microscopy (TEM) observations were carried out on JEOL JEM-2100F instrument operated at 200.0 kV. The electrophoresis studies of the TiO_2 nanoparticles were carried out on a Malvern Nano-ZS zetasizer at room temperature. In situ AFM measurements were conducted on a Nanowizard II (JPK Instruments, Berlin, Germany) between the interfaces of the silicon wafer and water with tapping mode using Si_3N_4 cantilevers (Veeco Instruments, CA) with a nominal spring constant of 0.58 N/m. Samples submitted to the in situ AFM observation were freshly fabricated on a polished silicon wafer. Ultraviolet illumination was produced by a medium-pressure mercury arc lamp (360 nm, ca. 20 mW/cm²). X-ray diffraction (XRD) patterns were measured on a Rigaku D/Max 2550 diffractometer (with Cu K α radiation, $\lambda = 1.5418\ \text{\AA}$) with polished single-crystalline silicon as substrates.

RESULTS AND DISCUSSION

Nondrying LbL Assembly of (Silicate/ TiO_2)* n_{ND} Films.

The as-synthesized TiO_2 nanoparticles have an average size of ca. 5.0 nm, as revealed by TEM measurements (see the Supporting Information, Figure S1). Electrophoresis study reveals that the ζ potential of the TiO_2 nanoparticles is +17 mV in aqueous colloidal suspension of pH 2.5. Sodium silicate is a common, inexpensive, and negatively charged chemical consisting of linear, branched, and ring-shaped oligomers (its chemical structure is shown in the inset of Figure 1a).²¹ Based on electrostatic interaction as the driving force, the positively charged TiO_2 nanoparticles can alternately deposit with sodium silicate by the nondrying LbL assembly to fabricate (silicate/ TiO_2)* n_{ND} composite films on PDPA-modified quartz or silicon substrates. The thicknesses of the (silicate/ TiO_2)* n_{ND} films deposited on quartz substrates with different deposition cycles were determined from their cross-sectional SEM images. As shown in Figure 1a, the thickness of the silicate/ TiO_2 films increases almost linearly with the number of film deposition cycles except for the first several cycles, with an average thickness increment of ca. 28.6 nm per deposition cycle. The initial nonlinear deposition originates from the influence of quartz substrate surfaces. The inset in Figure 1a shows the cross-sectional SEM image of a (silicate/ TiO_2)*50 $_{\text{ND}}$ film on quartz substrate, which has a constant thickness of ca. 1.43 μm . UV–vis absorption spectra were also employed to characterize the deposition process of silicate/ TiO_2 films. Figure 1b depicts

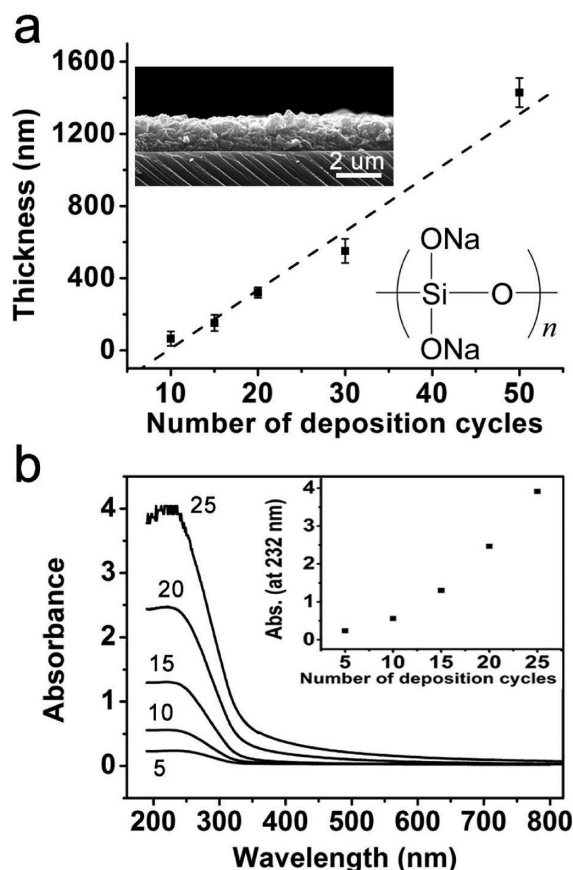


Figure 1. (a) Dependence of the thickness of $(\text{silicate}/\text{TiO}_2)_{n_{\text{ND}}}$ films on the number of deposition cycles. Insets are the cross-sectional SEM image of a $(\text{silicate}/\text{TiO}_2)_{50_{\text{ND}}}$ film (top) and chemical structure of sodium silicate (bottom). (b) UV-vis absorption spectra of $(\text{silicate}/\text{TiO}_2)_{n_{\text{ND}}}$ films with different deposition cycles on quartz substrates. The inset shows the absorbance at 232 nm as a function of the number of deposition cycles.

the UV-vis absorption spectra of silicate/ TiO_2 films with different deposition cycles on quartz substrates. All spectra have an absorption peak near 232 nm. The absorbance at 232 nm, which is the characteristic absorption of TiO_2 nanoparticles, increases linearly with the increase of deposition cycles of $(\text{silicate}/\text{TiO}_2)_{n_{\text{ND}}}$ films, except for the initial several cycles, as revealed in the inset of Figure 1b. It should be noted that the absorption spectra of $(\text{silicate}/\text{TiO}_2)_{n_{\text{ND}}}$ films with more than 25 deposition cycles cannot be obtained by UV-vis absorption spectroscopy measurements because the absorbance of these films saturates the current UV-vis spectrophotometer at the peak region. The linear growth of the $(\text{silicate}/\text{TiO}_2)_{n_{\text{ND}}}$ films provides a convenient way to tailor the desired film thickness by simply varying the number of film deposition cycles. EDX spectroscopy measurement of the powders scraped from the $(\text{silicate}/\text{TiO}_2)_{50_{\text{ND}}}$ film (Supporting Information, Figure S2) shows the signals of titanium and silicon at 4.52 and 1.74 keV, respectively, confirming that the films are composed of TiO_2 nanoparticles and sodium silicate. The atomic ratio of titanium to silicon is calculated to be 1.6:1. XRD patterns of the $(\text{silicate}/\text{TiO}_2)_{50_{\text{ND}}}$ film deposited on polished single-crystalline silicon (100) also demonstrate the existing of the TiO_2 nanoparticles in the film and further reveal that the TiO_2 nanoparticles in the film are anatase (Supporting Information, Figure S3).

The surface morphologies of the nondrying LbL assembled $(\text{silicate}/\text{TiO}_2)_{n_{\text{ND}}}$ films with different deposition cycles were investigated by SEM measurements. As shown in Figure 2a,

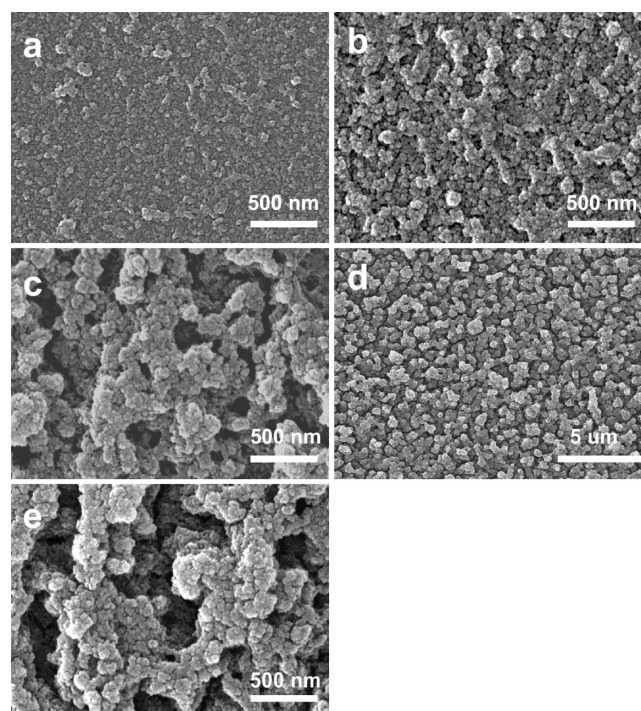


Figure 2. SEM images of $(\text{silicate}/\text{TiO}_2)_{n_{\text{ND}}}$ films fabricated by the nondrying LbL assembly on quartz substrates with n being (a) 5, (b) 10, (c) 20, and (d) 50. (e) is the magnified view of (d).

aggregates of nanoparticles with the size of 30–60 nm are observable on the surface of $(\text{silicate}/\text{TiO}_2)_{5_{\text{ND}}}$ film. These aggregates are the aggregated silicate and TiO_2 nanoparticles held together by electrostatic interaction between them derived from their alternate deposition. The amount of silicate and TiO_2 nanoparticles deposited in the $(\text{silicate}/\text{TiO}_2)_{5_{\text{ND}}}$ film is low as revealed by the film thickness measurements in Figure 1a. As more cycles of silicate/ TiO_2 films are deposited, the size and the amount of the aggregated particles deposited increase gradually. The loose stack of the aggregates of silicate and TiO_2 nanoparticles in the LbL assembled $(\text{silicate}/\text{TiO}_2)_{n_{\text{ND}}}$ films produces three-dimensional (3D) porous films, which can be clearly recognized in Figure 2b–e. The porous structures in the highly porous $(\text{silicate}/\text{TiO}_2)_{20_{\text{ND}}}$ and $(\text{silicate}/\text{TiO}_2)_{50_{\text{ND}}}$ films are quite similar, which is consistent with the linear deposition of the silicate/ TiO_2 films observed in Figure 1. The SEM image in Figure 2d confirms that the 1.43 μm thick porous $(\text{silicate}/\text{TiO}_2)_{50_{\text{ND}}}$ films are crack-free with large areas.

Drying LbL Assembly of $(\text{Silicate}/\text{TiO}_2)_{n_{\text{D}}}$ Films.

Drying LbL assembly was also employed to prepare the $(\text{silicate}/\text{TiO}_2)_{n_{\text{D}}}$ composite films, where a N_2 drying step was conducted after each layer deposition. UV-vis spectroscopy was used to monitor the deposition process of $(\text{silicate}/\text{TiO}_2)_{n_{\text{D}}}$ films with the drying steps. As shown in Figure 3a, all spectra have an absorption peak near 232 nm similar to that in Figure 1b. The absorbance at 232 nm increases linearly with the number of the film deposition cycles as indicated in the inset of Figure 3a, confirming the linear growth of the $(\text{silicate}/\text{TiO}_2)_{n_{\text{D}}}$ films. For a $(\text{silicate}/\text{TiO}_2)_{50_{\text{D}}}$ film, the absorbance at

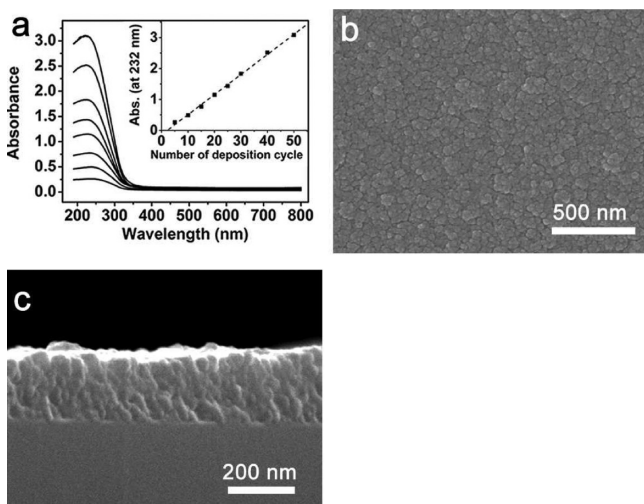


Figure 3. (a) UV-vis absorption spectra of $(\text{silicate}/\text{TiO}_2) \cdot n_{\text{D}}$ films fabricated by drying LbL assembly with different deposition cycles on quartz substrates. Inset shows the absorbance at 232 nm as a function of the number of deposition cycles. Top-view (b) and cross-sectional (c) SEM images of a $(\text{silicate}/\text{TiO}_2) \cdot 50_{\text{D}}$ film.

232 nm is ca. 3.1, which is even much smaller than that of the $(\text{silicate}/\text{TiO}_2) \cdot 25_{\text{ND}}$ film fabricated with the nondrying LbL assembly process. Therefore, the drying LbL assembly produces a thinner silicate/ TiO_2 film than the nondrying LbL assembly when the deposition cycles are the same. The top-view and cross-sectional SEM images of the $(\text{silicate}/\text{TiO}_2) \cdot 50_{\text{D}}$ film are shown in Figures 3b and 3c, respectively. The $(\text{silicate}/\text{TiO}_2) \cdot 50_{\text{D}}$ film has a smooth surface and compact film structure, which is quite different from these of the $(\text{silicate}/\text{TiO}_2) \cdot 50_{\text{ND}}$ film. The $(\text{silicate}/\text{TiO}_2) \cdot 50_{\text{D}}$ film has a thickness of ca. 208.5 nm, with one cycle of silicate/ TiO_2 film being ca. 4.2 nm. This value is much smaller than ca. 28.6 nm for the thickness of one cycle of silicate/ TiO_2 fabricated by the nondrying LbL assembly.

Influence of Drying and Nondrying Steps on the Fabrication of Silicate/ TiO_2 Films. The above results clearly show that the nondrying and the drying LbL assembly produce silicate/ TiO_2 films of quite different structures. To clarify the influence of drying and nondrying steps on the film structures, in situ AFM measurements were employed to characterize the surface morphologies of silicate/ TiO_2 films fabricated with and without drying steps. Samples submitted to the in situ AFM measurements were freshly prepared. After a layer of sodium

silicate or TiO_2 nanoparticles was deposited followed by water rinsing and N_2 or non- N_2 drying steps, the films were immediately placed in the AFM liquid cell containing water and the surface morphologies of these films were recorded. Figure 4a is the AFM image of a layer of silicate with a N_2 drying step on PDDA-modified silicon wafer. The silicate layer is smooth with a root-mean-square (rms) roughness of 1.0 nm. The nondrying deposition of TiO_2 nanoparticles leads to a rough $[\text{silicate}_{\text{D}} + \text{TiO}_{2\text{ND}}]$ film with a rms roughness being 2.1 nm. The island-like aggregated TiO_2 nanoparticles are clearly seen on the $[\text{silicate}_{\text{D}} + \text{TiO}_{2\text{ND}}]$ film (Figure 4b). In contrast, the $[\text{silicate}_{\text{D}} + \text{TiO}_{2\text{D}}]$ film with the TiO_2 layer being dried with N_2 flow has a quite smooth surface, with a rms roughness of 1.1 nm (Figure 4c). Similar to TiO_2 layers, the silicate layers deposited by the nondrying LbL assembly have a rougher surface than those deposited by the drying LbL assembly. As shown in Figures 4d and 4e, the $[\text{silicate}_{\text{D}} + \text{TiO}_{2\text{D}} + \text{silicate}_{\text{ND}}]$ and the $[\text{silicate}_{\text{D}} + \text{TiO}_{2\text{D}} + \text{silicate}_{\text{D}}]$ films have a rms roughness of 3.6 and 1.4 nm, respectively. The island-like aggregates of silicates are flattened after being drying with N_2 flow. Furthermore, the $[\text{silicate}_{\text{ND}} + \text{TiO}_{2\text{ND}}]$ film (with a rms roughness of 3.1 nm, Figure 4f) is rougher than the $[\text{silicate}_{\text{D}} + \text{TiO}_{2\text{ND}}]$ film (with a rms roughness of 2.1 nm, Figure 4b), demonstrating that the roughening effect of the nondrying LbL assembly can be enlarged when more layers are deposited.

From the in situ AFM measurements, it can be concluded that the sodium silicate and TiO_2 nanoparticles are deposited in their aggregated forms. Sodium silicate aggregates more easily with the decrease of solution pH. The water used in the rinsing steps has a pH of ~ 6.2 , which is much lower than the pH of the sodium silicate dipping solution. Therefore, aside from the silicate aggregates formed in aqueous sodium silicate solution, the water rinsing step can also induce the aggregation of the adsorbed silicates. Without the drying steps, aggregates of silicate and TiO_2 nanoparticles are retained in the $(\text{silicate}/\text{TiO}_2) \cdot n_{\text{ND}}$ films because of the rigid nature of TiO_2 nanoparticles and sodium silicate, as verified in Figures 4b and Figure 4d. As illustrated in Scheme 1a, the loose stack of the aggregated silicate and TiO_2 nanoparticles during the nondrying LbL assembly process produces porous silicate/ TiO_2 films. Although the amount of deposited silicate and TiO_2 nanoparticles in the beginning several deposition cycles is small, the roughness of the $(\text{silicate}/\text{TiO}_2) \cdot n_{\text{ND}}$ films increases with increasing number of film deposition cycles. The increased surface roughness permits more aggregates of TiO_2 nanoparticles and sodium silicate to deposit than in the previous

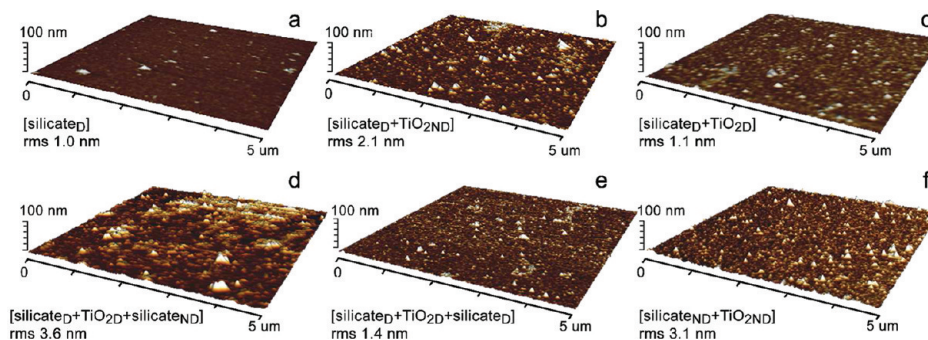
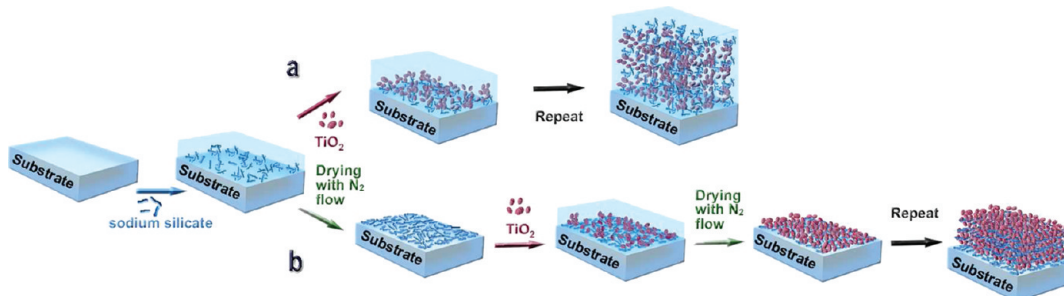


Figure 4. In situ AFM images of silicate/ TiO_2 films with different deposition cycles fabricated on silicon wafers with or without drying steps: (a) $[\text{silicate}_{\text{D}}]$, (b) $[\text{silicate}_{\text{D}} + \text{TiO}_{2\text{ND}}]$, (c) $[\text{silicate}_{\text{D}} + \text{TiO}_{2\text{D}}]$, (d) $[\text{silicate}_{\text{D}} + \text{TiO}_{2\text{D}} + \text{silicate}_{\text{ND}}]$, (e) $[\text{silicate}_{\text{D}} + \text{TiO}_{2\text{D}} + \text{silicate}_{\text{D}}]$, (f) $[\text{silicate}_{\text{ND}} + \text{TiO}_{2\text{ND}}]$. The rms of the films is shown in the lower left of the corresponding AFM images.

Scheme 1. Illustration of the Nondrying (a) and Drying (b) LbL Assembly for the Fabrication of Silicate/TiO₂ Composite Films

deposition cycle. Finally, highly porous silicate/TiO₂ films with large thickness are fabricated with a nondrying LbL assembly process. In contrast, N₂ drying after each layer deposition enables the fabrication of thin silicate/TiO₂ films with smooth surface and compact structures. As illustrated in Scheme 1b, we believe that a drying step with N₂ flow has at least two effects on the evolution of the deposited sodium silicate and TiO₂ nanoparticles, as follows: (i) N₂ flow can produce a lateral shearing force, which drives the spread of the aggregated silicate and/or TiO₂ nanoparticles. (ii) The dehydration of the aggregated silicate and/or TiO₂ nanoparticles and the capillary forces induced by the water evaporation in the drying process can result in the collapse and fusion of the aggregates and produce a compact and thin layer. Therefore, a N₂ drying step can disintegrate the aggregated silicate and TiO₂ nanoparticles to produce thin (silicate/TiO₂)**n_D* films with smooth surface and compact structures.

The extreme difference in drying and nondrying LbL assembled silicate/TiO₂ films originates from the high rigidity of silicate and TiO₂ nanoparticles. To confirm this point, LbL assembled poly(acrylic acid) (PAA)/TiO₂ films were fabricated with and without N₂ drying steps by replacing sodium silicate with flexible PAA. The fabrication of (PAA/TiO₂)**n_{ND}* and (PAA/TiO₂)**n_D* films are similar to those of (silicate/TiO₂)**n_{ND}* and (silicate/TiO₂)**n_D* films, with aqueous sodium silicate solution being replaced with aqueous PAA solution (1.0 mg/mL pH = 11.4). As shown in Figures 5a and 5c, both

the (PAA/TiO₂)*50_D and the (PAA/TiO₂)*50_{ND} films fabricated with and without the drying steps exhibit smooth surfaces and compact film structures. The thickness of the (PAA/TiO₂)*50_D and the (PAA/TiO₂)*50_{ND} films determined from their corresponding cross-sectional SEM images (Figures 5b and 5d) is ca. 77.7 nm and ca. 112.3 nm, respectively. The difference of the (PAA/TiO₂)*50_D and the (PAA/TiO₂)*50_{ND} films only lies in the film thickness. Similar to silicate/TiO₂ films, the aggregated TiO₂ nanoparticles are well retained in the (PAA/TiO₂)*50_{ND} films but disintegrated in the (PAA/TiO₂)*50_D films. Therefore, the (PAA/TiO₂)*50_{ND} films have a larger thickness than the (PAA/TiO₂)*50_D films. However, the (PAA/TiO₂)*50_{ND} films with compact structures are quite different with the highly porous (silicate/TiO₂)*50_{ND} films. Different from rigid sodium silicate aggregates, the flexible PAA can spontaneously adjust its configuration to fill in the interstices produced by the deposited aggregates of TiO₂ nanoparticles during the nondrying LbL assembly process. As a result, the nondrying LbL assembly of flexible PAA and rigid aggregates of TiO₂ nanoparticles produces thin and compact (PAA/TiO₂)**n_{ND}* films. In contrast, the silicate aggregates with high rigidity prohibit the configuration adjusting and lead to highly porous (silicate/TiO₂)**n_{ND}* films. The concentration-dependent deposition of (silicate/TiO₂)**n_{ND}* films further demonstrates that building blocks with properly large dimensions are also important for the fabrication of porous films by the nondrying LbL assembly. The aggregation of the sodium silicate in aqueous solutions is concentration-dependent. Figure 6 shows the SEM images of (silicate/TiO₂)*50_{ND} films fabricated by using aqueous sodium silicate solutions of 30.8, 15.4, and 7.7 mM. Combined with the (silicate/TiO₂)*50_{ND} film in Figure 2d (fabricated with a sodium silicate solution with concentration of 154 mM), it is clear that the porosity and the thickness of the (silicate/TiO₂)*50_{ND} films decrease with decreasing concentration of aqueous sodium silicate solutions. The interaction of silicates weakens in sodium silicate solution of low concentration. Therefore, less-aggregated silicates are deposited during the nondrying LbL assembly of sodium silicate and TiO₂ nanoparticles, producing silicate/TiO₂ films of smooth surface and thin thickness. The thicknesses of (silicate/TiO₂)*50 films fabricated by using aqueous sodium silicate solutions of 30.8, 15.4, and 7.7 mM are ~811.6, 427.9, and 207.5 nm, respectively, as determined from the cross-sectional SEM images in Figures 6c, 6f, and 6i.

Application of Highly Porous Silicate/TiO₂ Films for Dye Removal. Wastewater containing organic dyes generated by the textile industry has been regarded as one of the most harmful industrial pollutions. Generally, porous materials with large specific surface areas are used as the adsorbents to remove dyes from wastewater.²² As an example of application, the

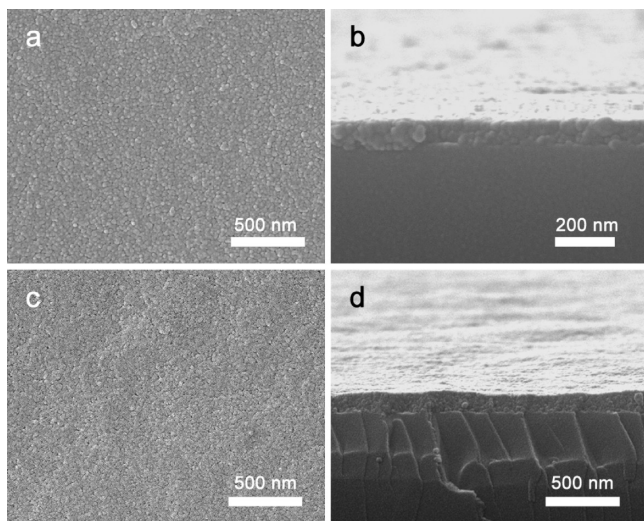


Figure 5. Top-view and cross-sectional SEM images of (PAA/TiO₂)*50 films fabricated by the drying (a, b) and nondrying (c, d) LbL assembly.

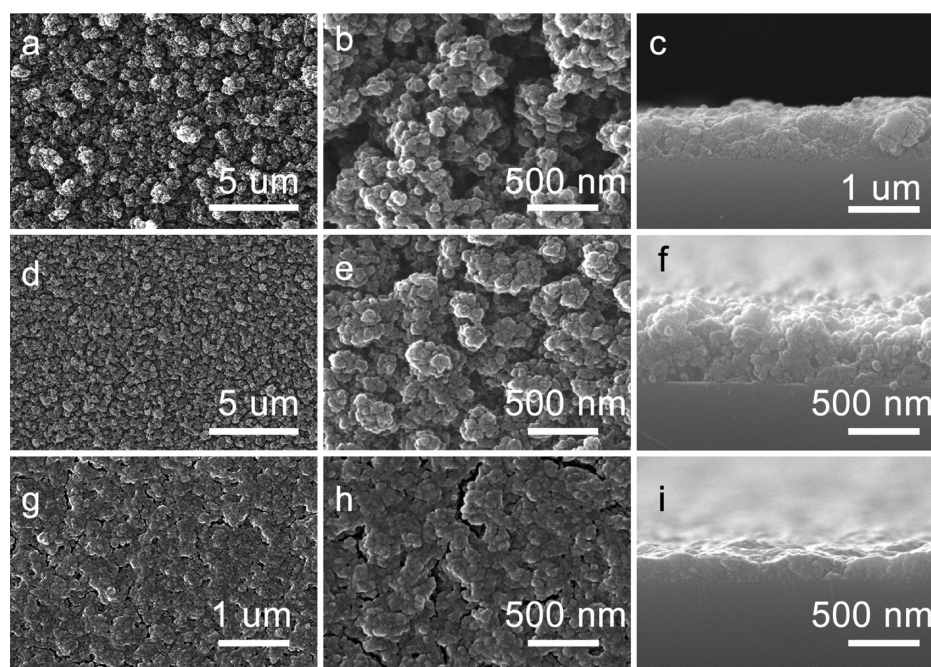


Figure 6. Top-view and cross-sectional SEM images of nondrying LbL assembled (silicate/TiO₂)*50_{ND} films fabricated with different concentrations of sodium silicate solutions: (a, b, c) 30.8 mM; (d, e, f) 15.4 mM; (g, h, i) 7.7 mM.

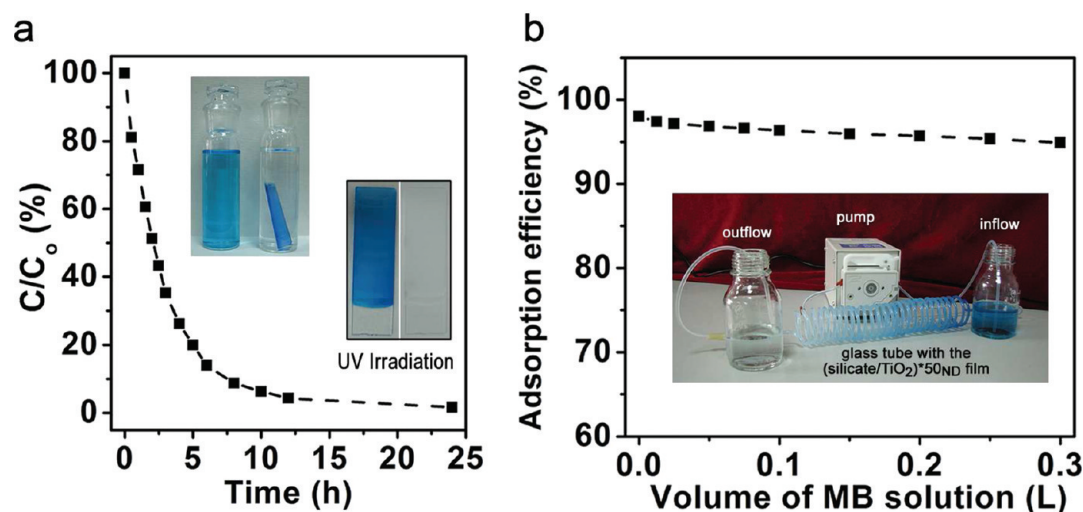


Figure 7. (a) Time-dependent adsorption profiles of MB molecules in a porous (silicate/TiO₂)*50_{ND} film. Insets of (a) show an aqueous MB solution before and after the removal of MB by the (silicate/TiO₂)*50_{ND} film and the UV irradiation-based recovery of the MB-adsorbed (silicate/TiO₂)*50_{ND} film, respectively. (b) Dye removal efficiency of a helical glass tube with its inner wall deposited with a (silicate/TiO₂)*50_{ND} film as a function of the flux volume of MB solution (10 μM, 2.5 mL/min). Inset in (b) shows the photograph of the real-time dye removal.

highly porous silicate/TiO₂ films fabricated by the nondrying LbL assembly were used as film adsorbents in wastewater purification. A quartz substrate (15 × 40 mm²) deposited on both sides with highly porous (silicate/TiO₂)*50_{ND} films were immersed into an aqueous methyl blue (MB) solution (15 mL, 10 μM), and the concentration of the MB solution was then monitored by recording the characteristic absorption of MB molecules at 664 nm. Figure 7a shows the time-dependent adsorption profile of the MB molecules into the silicate/TiO₂ films. Within the first 5 h, more than 80% of the MB molecules are removed by the (silicate/TiO₂)*50 films. After 24 h adsorption, more than 99% of MB molecules in the solution are removed, and the initial blue solution is apparently colorless as can be seen in the inset of Figure 7a. As also shown in the inset

of Figure 7a, the blue (silicate/TiO₂)*50 film with adsorbed MB returns to its initial colorless appearance after 21 min UV irradiation, confirming the complete decomposition of the MB molecules in the silicate/TiO₂ film. Upon UV irradiation, the anatase TiO₂ nanoparticles can generate electrons and holes, which then react with oxygen and water to produce the highly reactive species of superoxide anions and hydroxyl radicals, respectively.²³ These highly reactive species can degrade the adsorbed organic species and enable the reuse of the porous silicate/TiO₂ films. Because of the easy recovery of the film adsorbents upon the UV irradiation, the silicate/TiO₂ films can be repeatedly used for the removal of organic dyes from wastewater (Supporting Information, Figure S4). No peeling-off or dissolution of the silicate/TiO₂ films occurs during their

repeated usage for dye removal from wastewater, demonstrating that the films are mechanically robust. The silicate/TiO₂ films are also stable under sonication in water. The electrostatic interaction between the positively charged MB molecules and the negatively charged silicate is mainly responsible for the dye adsorption in silicate/TiO₂ films because the adsorption of negatively charged methyl orange into the silicate/TiO₂ films is unsuccessful. Other cationic dyes, such as crystal violet, rhodamine 6G, and acridine orange, can be removed by the porous silicate/TiO₂ films, demonstrating that the porous silicate/TiO₂ films are generally applicable for the removal of cationic dyes from wastewater.

One of the distinct advantages of the LbL assembly technique is its capability for depositing multilayer films on nonplanar substrates.¹² The porous (silicate/TiO₂)*50_{ND} film can be deposited on the inner wall of a helical glass tube (with an inner diameter of 3.0 mm and total length of 3.5 m) to simulate the industrial application of silicate/TiO₂ films in dye removal from wastewater (Figure 7b). An aqueous MB solution (10 μM) was pumped through the helical glass tube deposited with the (silicate/TiO₂)*50_{ND} film with a flux rate of 2.5 mL/min. As indicated in the inset of Figure 7b (and also in Supporting Information, Video S1), the outflow in the receiving bottle becomes colorless due to the effective adsorption of MB molecules within the porous (silicate/TiO₂)*50_{ND} film. UV–vis absorption spectroscopy determines that more than 98% of the MB molecules were adsorbed by the (silicate/TiO₂)*50_{ND} film in the initial stage, indicating the high removal efficiency of the silicate/TiO₂ films during the dye flowing process. As time passed, the dye removal efficiency decreases slightly due to the increased amount of dye adsorbed in the (silicate/TiO₂)*50_{ND} film. However, the adsorption efficiency still exceeds 95% after a total of 0.3 L MB solution is pumped through the tube. The above results show that under a flowing condition, the highly porous silicate/TiO₂ film still has a satisfactory ability of dye removal, promising its application in dye removal from wastewater.

CONCLUSIONS

In the present study, we have shown that drying and nondrying steps can be effectively employed to tailor the structures of LbL assembled films of sodium silicate and TiO₂ nanoparticles. Thick and highly porous silicate/TiO₂ films can be directly fabricated by the nondrying LbL assembly of oppositely charged sodium silicate and TiO₂ nanoparticles, while drying after each layer deposition leads to thin and compact silicate/TiO₂ films. The porous silicate/TiO₂ films are mechanically stable for cyclic usage as adsorbents to remove dyes from wastewater. The large difference of the drying and nondrying LbL assembled silicate/TiO₂ films has been reasonably ascribed to the rigidity and large dimensions of the building blocks as they are deposited in their aggregated forms. We believe that the principles disclosed in the present work can be extended to other LbL assembled systems and are useful for exploring the drying and nondrying steps to finely tailor the structure and functions of the LbL assembled films. Particularly, the nondrying LbL assembly of rigid building blocks of proper dimensions provides a facile way to directly fabricate various kinds of functional porous films which avoids the uses of porogens and tedious post-treatment steps.

ASSOCIATED CONTENT

Supporting Information

TEM image of TiO₂ nanoparticles; EDX spectra of the (silicate/TiO₂)*50_{ND} film; X-ray diffraction (XRD) patterns of the (silicate/TiO₂)*50_{ND} film; multiple usage of a (silicate/TiO₂)*50_{ND} film in MB removal; video of real-time removal of dyes by the helical glass tube coated with the (silicate/TiO₂)*50_{ND} film. This material is available free of charge via the Internet at <http://pubs.acs.org>.

AUTHOR INFORMATION

Corresponding Author

*E-mail: sun_junqi@jlu.edu.cn. Fax: 0086-431-85193421.

ACKNOWLEDGMENTS

This work is supported by the National Natural Science Foundation of China (NSFC Grants 20974037 and 20921003) and the State Key Laboratory of Advanced Technology for Materials Synthesis and Processing (Wuhan University of Technology).

REFERENCES

- (1) Decher, G. *Science* **1997**, *277*, 1232–1237.
- (2) (a) Hammond, P. T. *Adv. Mater.* **2004**, *16*, 1271–1293. (b) Quinn, J. F.; Johnston, A. P. R.; Such, G. K.; Zelikin, A. N.; Caruso, F. *Chem. Soc. Rev.* **2007**, *36*, 707–718. (c) Zhang, X.; Chen, H.; Zhang, H. Y. *Chem. Commun.* **2007**, 1395–1405. (d) Srivastava, S.; Kotov, N. A. *Acc. Chem. Res.* **2008**, *41*, 1831–1841. (e) Lavalle, P.; Voegel, J. C.; Vautier, D.; Senger, B.; Schaaf, P.; Ball, V. *Adv. Mater.* **2011**, *23*, 1191–1221.
- (3) (a) Fischer, P.; Koetse, M.; Laschewsky, A.; Wischerhoff, E.; Jullien, L.; Persoons, A.; Verbiest, T. *Macromolecules* **2000**, *33*, 9471–9473. (b) Van Cott, K. E.; Guzy, M.; Neyman, P.; Brands, C.; Heflin, J. R.; Gibson, H. W.; Davis, R. M. *Angew. Chem., Int. Ed.* **2002**, *41*, 3236–3238. (c) Kang, E. H.; Jin, P. C.; Yang, Y. Q.; Sun, J. Q.; Shen, J. C. *Chem. Commun.* **2006**, 4332–4334.
- (4) (a) Zhang, X.; Shi, F.; Yu, X.; Liu, H.; Fu, Y.; Wang, Z. Q.; Jiang, L.; Li, X. Y. *J. Am. Chem. Soc.* **2004**, *126*, 3064–3065. (b) Zhai, L.; Cebeci, F. C.; Cohen, R. E.; Rubner, M. F. *Nano Lett.* **2004**, *4*, 1349–1353. (c) Jisr, R. M.; Rmaile, H. H.; Schlenoff, J. B. *Angew. Chem., Int. Ed.* **2005**, *44*, 782–785. (d) Ji, J.; Fu, J. H.; Shen, J. C. *Adv. Mater.* **2006**, *18*, 1441–1444. (e) Li, Y.; Liu, F.; Sun, J. Q. *Chem. Commun.* **2009**, 2730–2732.
- (5) (a) Lvov, Y.; Caruso, F. *Anal. Chem.* **2001**, *73*, 4212–4217. (b) Calvo, E. J.; Danilowicz, C.; Woloski, A. J. *Am. Chem. Soc.* **2002**, *124*, 2452–2453. (c) Wegerich, F.; Turano, P.; Allegrozzi, M.; Möhwald, H.; Lisdat, F. *Langmuir* **2011**, *27*, 4202–4211.
- (6) (a) Chung, A. J.; Rubner, M. F. *Langmuir* **2002**, *18*, 1176–1183. (b) Serizawa, T.; Matsukuma, D.; Nanameki, K.; Uemura, M.; Kurusu, F.; Akashi, M. *Macromolecules* **2004**, *37*, 6531–6536. (c) Serpe, M. J.; Yarmey, K. A.; Nolan, C. M.; Lyon, L. A. *Biomacromolecules* **2005**, *6*, 408–413. (d) Ren, K. F.; Ji, J.; Shen, J. C. *Bioconjugate Chem.* **2006**, *17*, 77–83. (e) Schmidt, D. J.; Moskowitz, J. S.; Hammond, P. T. *Chem. Mater.* **2010**, *22*, 6416–6425.
- (7) (a) Ma, Y.; Zhang, Y. Y.; Wu, B. S.; Sun, W. P.; Li, Z. G.; Sun, J. Q. *Angew. Chem., Int. Ed.* **2011**, *50*, 6254–6257. (b) Costa, R. R.; Custódio, C. A.; Arias, F. J.; Rodríguez-Cabello, J. C.; Mano, J. F. *Small* **2011**, *7*, 2640–2649. (c) Wang, X.; Liu, F.; Zheng, X. W.; Sun, J. Q. *Angew. Chem., Int. Ed.* **2011**, *50*, 11378–11381.
- (8) (a) Gao, M. Y.; Gao, M. L.; Zhang, X.; Yang, Y.; Yang, B.; Shen, J. C. *Chem. Commun.* **1994**, 2777–2778. (b) Schmitt, J.; Decher, G. *Adv. Mater.* **1997**, *9*, 61–65. (c) Mamedov, A. A.; Belov, A.; Giersig, M.; Mamedova, N. N.; Kotov, N. A. *J. Am. Chem. Soc.* **2001**, *123*, 7738–7739. (d) Lee, D.; Rubner, M. F.; Cohen, R. E. *Nano Lett.* **2006**, *6*, 2305–2312. (e) Podsiadlo, P.; Sui, L.; Elkasabi, Y.; Burgardt, P.; Lee,

- J.; Miryala, A.; Kusumaatmaja, W.; Carman, M. R.; Shtein, M.; Kieffer, J.; Lahann, J.; Kotov, N. A. *Langmuir* **2007**, *23*, 7901–7906.
- (9) (a) Kong, W.; Zhang, X.; Gao, M. L.; Zhou, H.; Li, W.; Shen, J. C. *Macromol. Rapid Commun.* **1994**, *15*, 405–409. (b) Lvov, Y.; Ariga, K.; Ichinose, I.; Kunitake, T. *J. Am. Chem. Soc.* **1995**, *117*, 6117–6123. (c) Picart, C.; Lavalle, Ph.; Hubert, P.; Cuisinier, F. J. G.; Decher, G.; Schaaf, P.; Voegel, J.-C. *Langmuir* **2001**, *17*, 7414–7424. (d) Serizawa, T.; Yamaguchi, M.; Akashi, M. *Macromolecules* **2002**, *35*, 8656–8658. (e) Yoo, P. J.; Nam, K. T.; Qi, J.; Lee, S. K.; Park, J.; Belcher, A. M.; Hammond, P. T. *Nature Mater.* **2006**, *5*, 234–240.
- (10) (a) Zhang, X.; Gao, M. L.; Kong, X. X.; Sun, Y. P.; Shen, J. C. *Chem. Commun.* **1994**, 1055–1056. (b) Ariga, K.; Lvov, Y.; Kunitake, T. *J. Am. Chem. Soc.* **1997**, *119*, 2224–2231. (c) Advincula, R. C.; Fells, E.; Park, M. K. *Chem. Mater.* **2001**, *13*, 2870–2878.
- (11) (a) Guo, Y. M.; Geng, W.; Sun, J. Q. *Langmuir* **2009**, *25*, 1004–1010. (b) Li, Y.; Li, L.; Sun, J. Q. *Angew. Chem., Int. Ed.* **2010**, *49*, 6129–6133. (c) Liu, X. K.; Zhou, L.; Liu, F.; Ji, M. Y.; Tang, W. G.; Pang, M. J.; Sun, J. Q. *J. Mater. Chem.* **2010**, *20*, 7721–7727. (d) Zhang, L.; Sun, J. Q. *Chem. Commun.* **2009**, 3901–3903. (e) Liu, X. K.; Dai, B. Y.; Zhou, L.; Sun, J. Q. *J. Mater. Chem.* **2009**, *19*, 497–504. (f) Zhang, L.; Sun, J. Q. *Macromolecules* **2010**, *43*, 2413–2420.
- (12) (a) Caruso, F.; Caruso, R. A.; Möhwald, H. *Science* **1998**, *282*, 1111–1114. (b) Ai, S.; Lu, G.; He, Q.; Li, J. *J. Am. Chem. Soc.* **2003**, *125*, 11140–11141. (c) Dotzauer, D. M.; Dai, J.; Sun, L.; Bruening, M. L. *Nano Lett.* **2006**, *6*, 2268–2272. (d) Ma, Y.; Sun, J. Q.; Shen, J. C. *Chem. Mater.* **2007**, *19*, 5058–5062. (e) Wang, Y.; Angelatos, A. S.; Caruso, F. *Chem. Mater.* **2008**, *20*, 848–858.
- (13) (a) Büscher, K.; Karlheinz, K.; Ahrens, H.; Helm, C. A. *Langmuir* **2002**, *18*, 3585–3591. (b) Tan, H. L.; McMurdo, M. J.; Pan, G.; Van Patten, P. G. *Langmuir* **2003**, *19*, 9311–9314. (c) Salomäki, M.; Vinokurov, I. A.; Kankare, J. *Langmuir* **2005**, *21*, 11232–11240.
- (14) (a) Decher, G.; Schmitt, J. *Prog. Colloid Polym. Sci.* **1992**, *89*, 160–164. (b) Lösche, M.; Schmitt, J.; Decher, G.; Bouwman, W. G.; Kjaer, K. *Macromolecules* **1998**, *31*, 8893–8906. (c) Dubas, S. T.; Schlenoff, J. B. *Macromolecules* **1999**, *32*, 8153–8160. (d) Schoeler, B.; Kumaraswamy, G.; Caruso, F. *Macromolecules* **2002**, *35*, 889–897. (e) Kovacevic, D.; van der Burgh, S.; de Keizer, A.; Stuart, M. A. C. *Langmuir* **2002**, *18*, 5607–5612.
- (15) Wang, Y.; Stedronsky, E.; Regen, S. L. *J. Am. Chem. Soc.* **2008**, *130*, 16510–16511.
- (16) (a) Shiratori, S. S.; Rubner, M. F. *Macromolecules* **2000**, *33*, 4213–4219. (b) Fu, J. H.; Ji, J.; Shen, L. Y.; Kueller, A.; Rosenhahn, A.; Shen, J. C.; Grunze, M. *Langmuir* **2009**, *25*, 672–675. (c) Peng, C. Q.; Thio, Y. S.; Gerhardt, R. A.; Ambaye, H.; Lauter, V. *Chem. Mater.* **2011**, *23*, 4548–4556.
- (17) Lee, S. W.; Kim, B.-S.; Chen, S.; Yang, S.-H.; Hammond, P. T. *J. Am. Chem. Soc.* **2009**, *131*, 671–679.
- (18) (a) Lvov, Y.; Ariga, K.; Onda, M.; Ichinose, I.; Kunitake, T. *Colloids Surf., A* **1999**, *146*, 337–346. (b) Chen, J.; Luo, G.; Cao, W. J. *Colloid Interface Sci.* **2001**, *238*, 62–69. (c) Halthur, T. J.; Claesson, P. M.; Elofsson, U. M. *J. Am. Chem. Soc.* **2004**, *126*, 17009–17015. (d) Patel, D. S.; Aithal, R. K.; Krishna, G.; Lvov, Y.; Tien, M.; Knila, D. *Colloids Surf., B* **2005**, *43*, 13–19. (e) Lourenco, J. M. C.; Ribeiro, P. A.; do Rego, A. M. B.; Raposo, M. J. *Colloid Interface Sci.* **2007**, *313*, 26–33.
- (19) Wang, L. M.; Wang, L.; Su, Z. H. *Soft Matter* **2011**, *7*, 4851–4855.
- (20) Choi, W.; Termin, A.; Hoffmann, M. R. *J. Phys. Chem.* **1994**, *98*, 13669–13679.
- (21) He, J. H.; Fujikawa, S.; Kunitake, T.; Nakao, A. *Chem. Mater.* **2003**, *15*, 3308–3313.
- (22) (a) Zhuang, X.; Wan, Y.; Feng, C.; Shen, Y.; Zhao, D. *Chem. Mater.* **2009**, *21*, 706–716. (b) Yan, Z.; Li, G. T.; Mu, L.; Tao, S. Y. *J. Mater. Chem.* **2006**, *16*, 1717–1725. (c) Zhong, L. S.; Hu, J. S.; Liang, H. P.; Cao, A. M.; Song, W. G.; Wan, L. J. *Adv. Mater.* **2006**, *18*, 2426–2631.
- (23) (a) Fujishima, A.; Honda, K. *Nature* **1972**, *238*, 37–38. (b) Linsebigler, A. L.; Lu, G.; Yates, J. T. *Chem. Rev.* **1995**, *95*, 735–758. (c) Fox, M. A.; Dulay, M. T. *Chem. Rev.* **1993**, *93*, 341–357.
- (d) Kamat, P. V. *J. Phys. Chem. C* **2007**, *111*, 2834–2860. (e) Zhang, H. J.; Chen, G. H.; Bahnemann, D. W. *J. Mater. Chem.* **2009**, *19*, 5089–5121.